Available online at www.sciencedirect.com
SCIENCE DIRECT®
Polymer 45 (2004) 2691–2710
polymer
www.elsevier.com/locate/polymer

Superstructural hierarchy developed in coupled high shear/high thermal gradient conditions of injection molding in nylon 6 nanocomposites

B. Yalcin, M. Cakmak*

Department of Polymer Engineering, University of Akron, Akron, OH 44325-0301, USA

Received 15 September 2003; received in revised form 30 December 2003; accepted 7 January 2004

Abstract

The spatial variation of the superstructure developed along and across the flow direction of injection-molded nylon 6 and its nanocomposites are presented using transmission polarized optical photomicrographs and micro-small-angle laser light scattering (SALS). At low mold temperature, 50 °C, the structure of unfilled nylon 6 is made up of steep structural gradient containing oriented threads at the surface surrounding undeformed spherulites in the interior. In nanocomposite samples, on the other hand, the development of complete spherulites is interrupted by high nucleation density caused by the presence of nanoparticles and shear amplification that occurs in small spaces between these particles. The latter phenomenon was found to be prevalent even at high mold temperatures where the cooling rates are greatly suppressed. In the structure gradient, polymer/nanocomposite samples show double shear regions near the surface surrounding the core regions that contain sheaves. The origin of complex superimposed SALS patterns is explained in terms of the short and long-range spatial correlations of these preferentially oriented sheaves and their optic axes.

Keywords: Injection molding; Nylon-6 nanocomposites; Small angle laser light scattering

1. Introduction

Over the last decade nanoparticles with platelet morphology have received special recognition in the polymer composites area. Nanoplatelet type fillers enhance mechanical properties [1–4] and impart improved permeability [5] and flammability [6] to the polymers, while maintaining high clarity and low weight. These property improvements are primarily due to an increased interfacial area between the thin and high aspect ratio nanoplatelets and polymers. Interaction between the filler and the polymer and, hence, the reinforcement is maximized when compatibility between the two is satisfied and the nanofillers are well dispersed in the polymer matrix [7].

Further reinforcement of the nanocomposites can be achieved through orientation of the fillers during processing operations, such as melt spinning [8], thin film casting [9] or injection molding [10]. The ability of nanoplatelets to orient in a flow field and impart high levels of orientation to the solidifying polymer melt in confined spaces result in crystallization conditions that produces highly anisotropic structures [11,12]. This is especially true for crystallizable polymers.

Nylon 6 is the first crystallizable polymer that has been reinforced by nanoparticles [13,14]. Many publications focused on the preparation techniques of nylon 6 nanocomposites [1–4,13,15–21]. There have also been a few attempts to understand the influence of processing conditions on the structural evolution and resulting properties in Nylon 6 and its nanocomposites [8,22–24]. In a previous paper, we reported the spatial variation of local crystalline orientation of nylon 6 and nanoparticles across the thickness of injection molded parts using a variety of characterization techniques, including microbeam WAXD/SAXS and TEM [25]. Nanoparticles were shown to orient preferentially in the flow direction and induce high levels of shear deformation resulting in high levels of orientation of nylon 6 chains throughout the thickness of the parts even at high mold temperatures. This was attributed to the shear amplification effect in the confined spaces between adjacent nanoparticles coupled with suppression of chain relaxation in the presence of nanoparticles. This behavior very much resembles the orientation behavior of thermotropic liquid

* Corresponding author.
E-mail address: cakmak@uakron.edu (M. Cakmak).

0032-3861/$ - see front matter © 2004 Elsevier Ltd. All rights reserved.
doi:10.1016/j.polymer.2004.01.031

crystalline polymers where the orientation relaxation is greatly suppressed [26,27].

In this study, we present the effect of nanoparticles on the superstructure development in nylon 6 macro crystals in the injection molded parts.

2. Experimental

2.1. Materials

Nylon 6 general-purpose homopolymer resin (Capron® 8202) and experimental nylon 6 packaging grade nanocomposite resin (Capron® XA-2744) with a density of 1.13 g/cm^3 were kindly provided in the form of pellets by Allied Signal Honeywell Corporation. Capron® XA-2744 was prepared at a loading of 5 wt% by melt compounding in a twin-screw extruder. The viscosity of the materials was measured at 250 °C using an Instron capillary rheometer.

2.2. Injection molding

The samples were injection molded with a Van Dorn (Model HP with a Pathfinder 1000 controller) 55 ton reciprocating-screw injection-molding machine equipped with an oil circulating mold temperature controller. The samples were molded into a standard type-1 D-638 ASTM end gated test specimen with a 3 mm thickness. The samples were prepared at two different mold temperatures (50, 130 °C) and injection speeds (2.02, 17 *cm/s*). The rest of the processing variables including melt temperature (250 °C), injection pressure (650 psi), screw rotation speed (100 rpm) and clamp closed time (1 min holding followed by cooling) were kept constant. Large end-gated injection molded tensile bars were chosen for all the analysis.

2.3. Sample sectioning

Three cutting procedures were used to section the samples. These cutting procedures are shown in Fig. 1. Procedure A consisted of cutting sections perpendicular to the flow direction in the TD–ND plane. In procedure B, the samples were sectioned parallel to the flow direction on the FD–ND plane along the center of the sample. Procedure C consisted of cutting sections from skin to core, parallel to flow direction on the FD–TD plane.

2.4. Differential scanning calorimeter

The differential scanning calorimeter (DSC) measurements were performed using a Dupont TA 2920. The samples were cut according to C-Cut procedure (FD–TD cut plane) and local thermal behavior was investigated at an interval of 100 μm from skin to core of the molded part at a heating rate of 20 °C/min in nitrogen atmosphere.

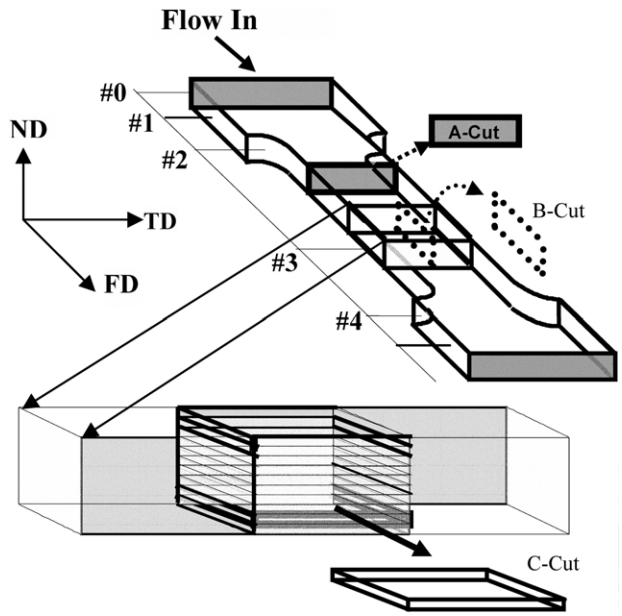

Fig. 1. Sample sectioning procedures.

2.5. Microbeam wide angle X-ray diffraction

Microbeam WAXS film patterns of nanocomposite samples were taken at a series of locations from skin to core in the FD–ND plane with X-ray beam directed along the transverse direction using the matrixing microbeam X-ray camera (MMBX) developed in our laboratory [28]. The camera was mounted on a 12 kW Rigaku rotating anode generator operated at 40 kV and 150 mA. A 50 μm diameter Cu Kα beam obtained using a nickel foil monochromator and a pinhole collimator allowed highly localized skin to core (1500 μm) mapping of the B-Cut samples with a precision $x-y$ translation stage.

2.6. Optical microscopy

2.6.1. Micrographs

Samples were cut according to A, B and C-Cut procedures using a Reichert–Jung 2050 microtome. They were then sandwiched between two glass slides and placed on a Leitz Laborlux 12 Pol S microscope stage oriented with their long axes at various angles to polarization directions of crossed polarizers. A first order red wave plate was also inserted with its slow axis oriented at 45° to the crossed polarizers. The arrangement of the sample, the cross-polarizers and red wave plate is illustrated schematically for each optical image. The pictures of the samples were taken with a DC 290 Kodak Zoom digital camera as well as Sony 3 Chip CCD camera connected to the optical microscope. The thickness of A and B cut samples were 20 μm and that of the C-Cut samples was 2 μm.

2.6.2. Birefringence measurement of B-Cut samples

The birefringence (Δn_{13}) (1 = flow direction, 3 =

thickness direction) was measured on B-Cut samples. Measurement was carried out with a Leitz Laborlux 12 POL S microscope with a thirty-order Berec compensator. The local symmetry axis direction was found to vary from skin to core in nanocomposite samples. Therefore, the local direction of the symmetry axis was measured first and maximum birefringence was determined with respect to this local symmetry axis.

The value of optical retardation Γ (mm) at 546 nm was obtained from the calibration chart of the compensator and the birefringence (Δn_{13}) was calculated using the equation below:

$$\Delta n_{13} = \Gamma/d \tag{2.1}$$

where d is the thickness of the sample (mm).

2.7. Small angle light scattering (SALS)

A 2 mW 632.8 nm He–Ne with beam size of 1 mm was used as the source of polarized monochromatic light. Molded samples were microtomed into a series of 20 μm thick layers from skin to core along the FD–TD plane of unfilled nylon. Due to very high nucleation density in the presence of nanoparticles, the latter thickness was reduced to 2 μm for molded Nylon 6 nanocomposites.

For SALS experiments the samples were immersed in a fluid with a refractive index of 1.532 and placed between two microscopic slides in order to suppress surface scattering. Hv patterns were obtained with the polarizer and analyzed oriented in TD and FD, respectively. Vv patterns were obtained with the polarizer parallel to the FD. On select sample H_H and V_H patterns were also obtained. The patterns were captured using an instant Polaroid camera and a 16-bit CCD camera software (Photometrics-cooled CCD) operated by IPLab spectrum.

Since there was no considerable deformation in unfilled nylon 6, the equivalent radius (R_0) of the spherulites was estimated using Eq. (2.2):

$$R = \lambda/[\pi \sin(\theta_{max}/2)] \tag{2.2}$$

3. Results and discussion

3.1. Differential scanning calorimeter

3.1.1. Preliminary thermal analysis on compression molded samples

In order to assess the nonisothermal crystallization behavior in the absence of flow, compression-molded samples were crystallized by cooling at a rate of 10 °C/min after holding 3 min at 250 °C (Fig. 2). The width of the crystallization peak for the nanocomposite is narrower and the crystallization peak appears at higher temperatures, as compared to unfilled nylon 6 matrix. This is due to increased number of nucleation sites offered by the

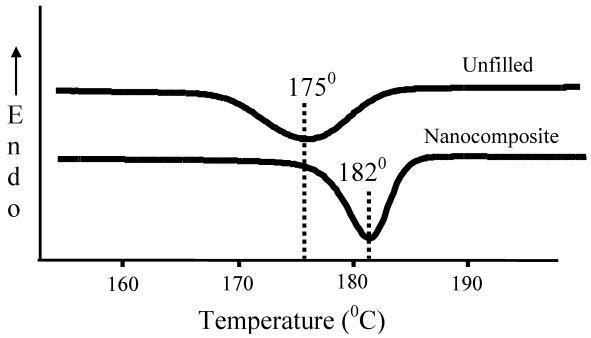

Fig. 2. DSC scans of unfilled and nanoparticle filled nylon 6 pellets: hot crystallization from above melting point to room temperature.

nanoparticles to the solidifying polymer melt. Upon heating, both filled and unfilled nylon 6 exhibit multiple melting peaks. In Fig. 3 unfilled nylon 6 crystals melt at around 220 °C with a small shoulder at 210 °C. Nanocomposite samples show three peaks at 210, 220 and 238 °C. The incorporation of nanoparticles increases the area under the 210 °C peak and reduces the area under the 220 °C peak. A third melting peak at 238 °C represents thermodynamically 'protected' Nylon 6 crystallites in the immediate vicinity of the nanoplatelets and in the galleries [29,30]. In an earlier work with the same material, we have shown that we have substantial intercalation of the nanoparticles in the nanocomposite samples before injection molding [25]. The two lower melting endotherms have been the subject of debate since White [31] reported them for nylon 66 yarns. The lower and higher melting peaks has been attributed to γ and the α phase of nylon 6, respectively [32,33]. Other studies [34,35] showed that these double melting peaks correspond to the superposition of the melting of the original crystals, recrystallization and the subsequent melting of the recrystallized crystals during the DSC heating. A recent study in our laboratories [8] combined thermal analysis and hot stage wide angle X-ray diffraction in order to observe the crystal forms of nylon 6 during heating. In this study it was shown that at room temperature the γ phase of nylon 6 crystals was dominant. At 190 °C, some of these γ crystals start to recrystallize into α phase and crystallization continues at

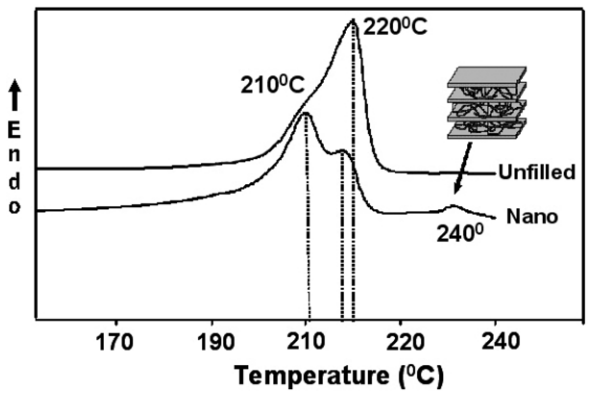

Fig. 3. DSC scans of unfilled and nanoparticle filed nylon 6 pellets: heating from room temperature to above melting point.

temperatures up to 212 °C. These crystals completely melt around 240 °C. The melting of γ crystals, on the other hand, occurs in 210–250 °C range. Thus, γ and α crystals melt simultaneously—a result that disagrees with the assignment of these peaks to γ and α crystals alone. [32,33].

3.1.2. Thermal analysis (injection molded samples)

Figs. 4 and 5 show the DSC scans and WAXD patterns of nylon 6 nanocomposite samples at various depths along the thickness direction for 130 and 50 °C mold temperatures, respectively. In an earlier study [25] we explained in detail the microbeam WAXD patterns taken along the thickness of the molded parts for unfilled nylon 6 and its nanocomposites. Nylon 6 exhibits two intense α diffraction peaks at 20.5 and 24° corresponding to (200) and the (002), (202) doublet and one weak γ peak at 21.5° belonging to (001 + 200). At low mold temperature and hence fast cooling rates, the γ phase of nylon 6 is promoted. For instance, at the mold temperature of 50 °C, the top 750 μm layer near the surface was found to consist mainly of γ phase. In this sample, the α phase preferentially grows in regions closer to the core of the molded part where relatively low cooling rates prevail.

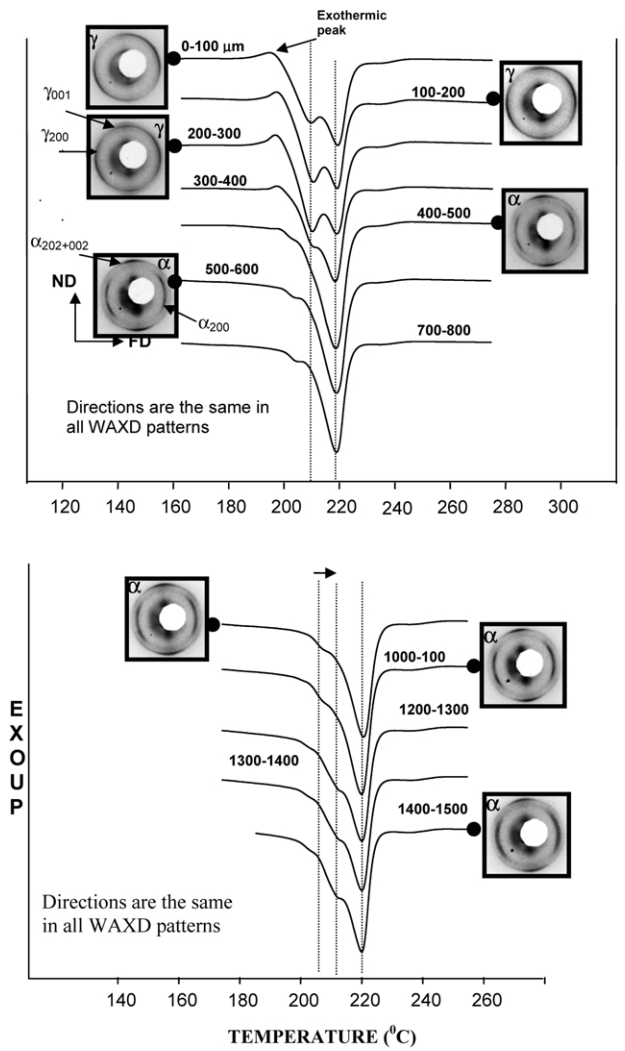

Fig. 4. Skin to core thermal behavior of nylon 6 nanocomposites along the thickness of injection molded parts (MT 130 °C, IS 2.02 cm/s). Distance from the surface of the molded parts and the corresponding WAXD patterns are indicated next to each figure.

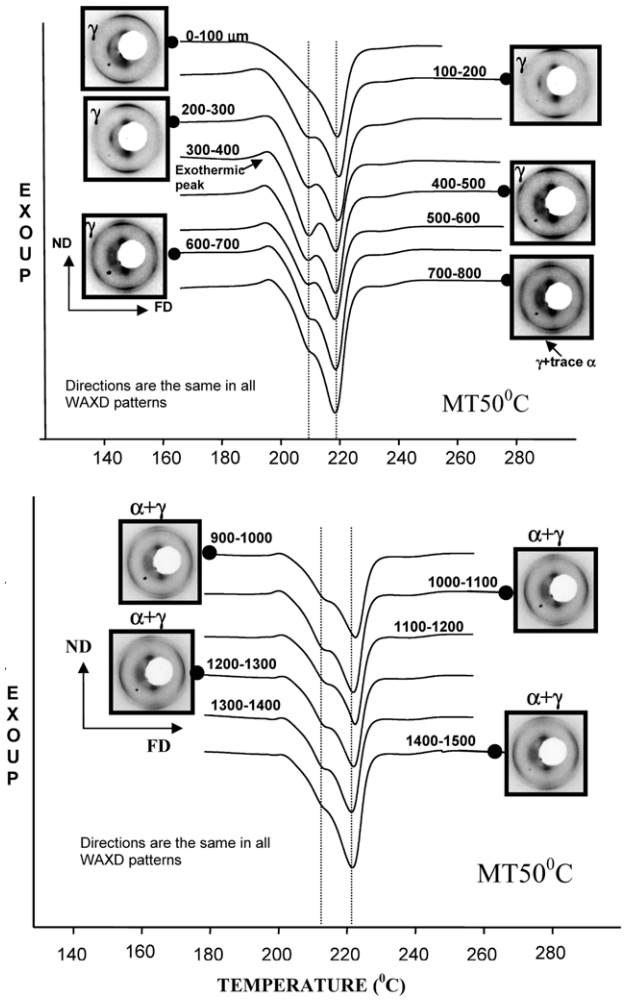

Fig. 5. Skin to core thermal behavior of nylon 6 nanocomposites along the thickness of injection molded parts (MT 50 °C, IS 2.02 cm/s). Distance from the surface of the molded parts and the corresponding WAXD patterns are indicated next to each figure.

When the mold temperature was increased to 130 °C, the pure γ phase surface layer thickness decreased to 300 μm. The rest of the interior was found to be all in the α phase. In the light of these results, double melting peaks are still observed close to skin regions where only the γ phase is present. This evidences once again that double melting peaks cannot be attributed to the different crystal phases of nylon 6. It is important to point out that we do not disregard the possibility of forming α-crystals during the DSC scan, but rather disagree with the idea of assigning its melting region to the high temperature melting endotherm, especially when we compare, for instance, the relative areas of the melting endotherms in 600–700 μm region (50 °C mold temperature case) possessing entirely γ phase initially and showing almost entirely a high temperature

endotherm during melting. It is physically unrealistic to imagine that all γ crystals would recrystallize to α form at such fast heating rates (20 °C/min). Our previous studies with hot stage WAXD do not indicate a change in the crystal type at high temperatures other than a minor amount of recrystallization provided that the heating rate is slow (3 °C/min). Other studies have also reported that well dispersed nylon 6 nanocomposites exhibiting entirely γ-phase at room temperature preserved their crystal form throughout the entire temperature range from ambient to melting, with no α-phase prior to melting [36].

In Figs. 4 and 5 a small exothermic peak around 195 °C is observed at various depths along the thickness direction. Reorganization of highly oriented amorphous regions or unstable crystals into a more stable form through crystallization could cause such sub-T_m peaks [8]. This minor sub melting exothermic peak is closely linked with the presence and magnitude of low temperature melting peak that is adjacent to this exotherm. As the area under the exothermic peak increases, so does the low temperature endotherm that increases its area. These sub-melting exothermic peaks are typically observed in the shear regions where the material has undergone substantial deformation under the severe shear forces that took place during the injection stage. This clearly suggests that these regions are not entirely stable and although they contain highly oriented crystalline regions, there is also a portion of highly oriented polymer chains that are presumably trapped between the nanoparticles and prevented from crystallizing due to steric hindrances. These chains are kept in this metastable stage until sufficient mobility is introduced to the material that occurs near the melting. Once this mobility is enhanced through temperature rise, these chains crystallize resulting in relatively disordered and/or small crystallites that eventually is partial source of the lower temperature endothermic peak. Towards the relatively relaxed core, the exothermic peak gradually decreases in size, disappears and slightly appears in the core region. As will be discussed in Section 3.2, whenever the exothermic peak appears we also see relatively larger birefringence that is a total measure of optical anisotropy. This is prevalent when those regions are formed under substantial shearing (e.g. 100–400 mm) and slightly in the core of the sample molded at 50C (1100–1200 μm). These observations suggest that the double melting peaks are due to the overlapping of the multiple phenomena, i.e. sub-T_m crystallization of the highly oriented amorphous chains and subsequent melting of the already present and newly formed crystals. Both crystal phases have the same equilibrium melting temperature [35] 273 °C and can melt concurrently either at high or low melting regions depending on their size and perfection.

Crystallinity profile in all of the processing conditions was observed to be relatively flat (around 25–30%) with a slight tendency to become lower near the skin particularly in low mold temperatures.

3.2. Birefringence distribution

3.2.1. Comparative section—unfilled vs. nanocomposite

In order to distinguish the structural gradient of the samples along the thickness direction, birefringence and tilt angle (defining the local symmetry axes) distribution is determined on the symmetry planes defining the part molded at 50 °C. Birefringence, which is a measure of optical anisotropy, is greatly influenced by the crystallinity and orientation levels of the system.

In Fig. 6 birefringence distribution for unfilled nylon 6 molded at 50 °C shows a maximum only near the surface region which is in agreement with our previous microbeam WAXD observation for this region [25]. Towards the interior, the birefringence values decrease and then show a slight increase towards the core. Nylon 6 nanocomposites, on the other hand, display fairly high birefringence levels not only near the surface but also in the interior. Double maxima of birefringence are observed near the surface. Birefringence shows a maximum at 125 μm below the surface. This first maximum is formed during the injection stage. The second maximum located 255 μm below the surface is formed during the packing stage under the influence of creeping flow and high pressures.

When the mold temperature is at 130 °C, nanocomposite samples still show high levels of orientation throughout the thickness of the samples. WAXD patterns in Fig. 4 support this observation.

It should be pointed out that the birefringence values presented here are the maximum birefringence at each location along the thickness of the sample whose local symmetry axis is defined by the extinction angle (tilt angle). These tilt angles display a fluctuating negative and positive

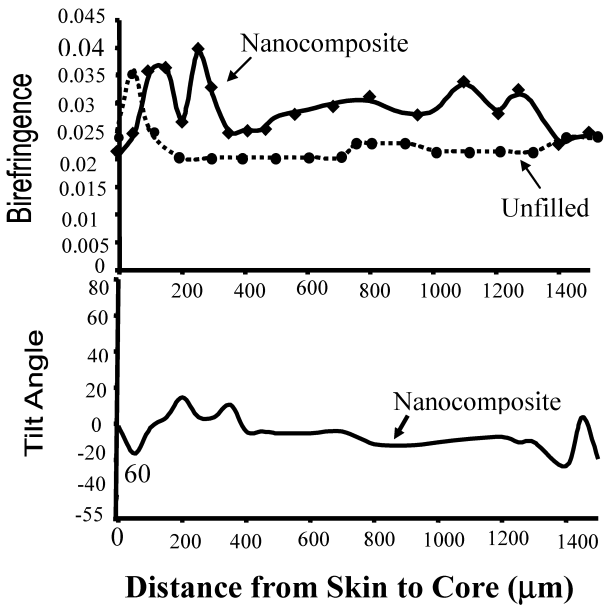

Fig. 6. Birefringence and tilt angle distribution of unfilled nylon 6 and its nanocomposite along with the optical birefringence patterns for samples molded at 50 °C.

values across the thickness representing complexity of structural gradient across the thickness. Although birefringence and tilt angle measurements assume that the local symmetry axis is on the FD–ND plane, we had found earlier that the chain axis does not necessarily lie on this plane but points out of plane in certain locations along the normal direction of the samples. However, the in-plane birefringence values and the corresponding tilt angles still give us an idea about the multi-layered morphology and their orientation levels. The details of the structural hierarchy should be established with direct morphological observations by optical photomicrographs.

4. Structural hierarchy

4.1. Polarized transmission photomicrographs

4.1.1. Optical images

The morphology of the unfilled sample molded at 130 °C is spherulitic even in the skin region. Such high temperatures apparently prevent the formation of the structural gradients containing highly oriented layers near the surface of injection-molded parts such as polypropylene [37].

The sample molded at 50 °C, on the other hand, displays mainly a three-layered structure, as shown in Fig. 7. The analysis of the structural layers was performed for B-Cut samples. The typical oriented skin layer that forms at the surface is very thin in nylon 6 due to its low viscosity. Therefore, the structural layer underneath the skin is considered to be the first layer in our investigations. The thickness of this layer is about 60 μm. It has a parabolic depth profile typical of shear flow, as evidenced by the spatial variation of extinction angle. As shown in Fig. 8(a) light extinction (black region) moves towards the interior as the sample is rotated from 0 to 45°. For each rotation angle the extinction regions are determined by the spatial location of the lowest intensity along the optical line cut from the surface to the interior. Fig. 8(b) shows this procedure for the sample that is rotated through 45°. The entire extinction angle profile is shown in Fig. 8(c). The symmetry axis in the top region is in the flow direction; towards the interior, the symmetry axis varies spatially with respect to the flow direction. In the middle of the first layer the symmetry axis is out of FD–ND plane as light extinction could not be achieved by rotation under crossed polarizers. This clearly evidences that this profile captures the geometrical features of the development of solidified layer during injection and parabolic profile of the shear field. Near the skin, the local symmetry axes are tilted towards the skin following the contour of the leading edge of the solid–liquid boundary and in the interior it follows the parabolic profile of the governing shear field.

A 70 μm thick second layer follows the first layer with a steep structural changeover. In Fig. 9 the polarized optical images of this structure with the first order red wave plate

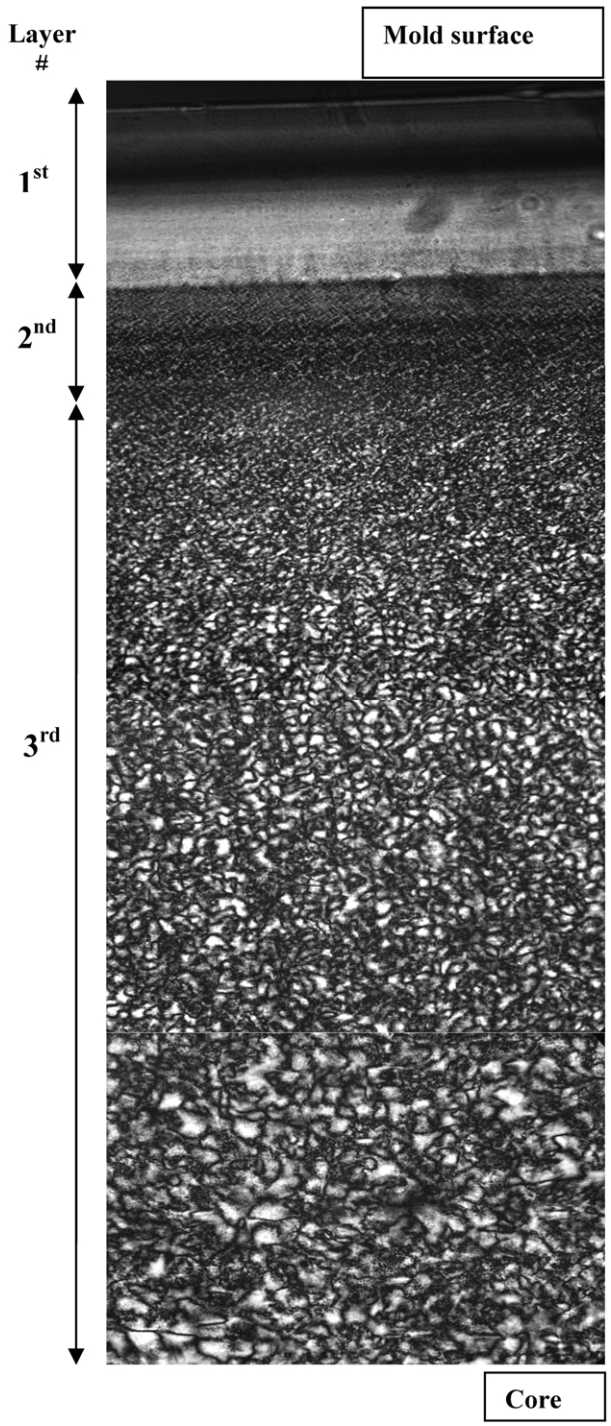

Fig. 7. Polarized optical transmission photomicrograph of A-Cut sample sectioned from injection molded nylon 6 molded at 50 °C.

are shown for a B-Cut sample for a series of rotations. When the FD of the sample is at 25° to one of the cross-polarizers, spherulite-like morphology is visible. When the FD of the sample is parallel or 45° to the cross-polarizers, the appearance change entirely into rod-like entities. Similar optical polarization behavior was shown by Stein [38] for sheaf-like structures of PCTFE–VF copolymers in the intermediate stages of the development of spherulites.

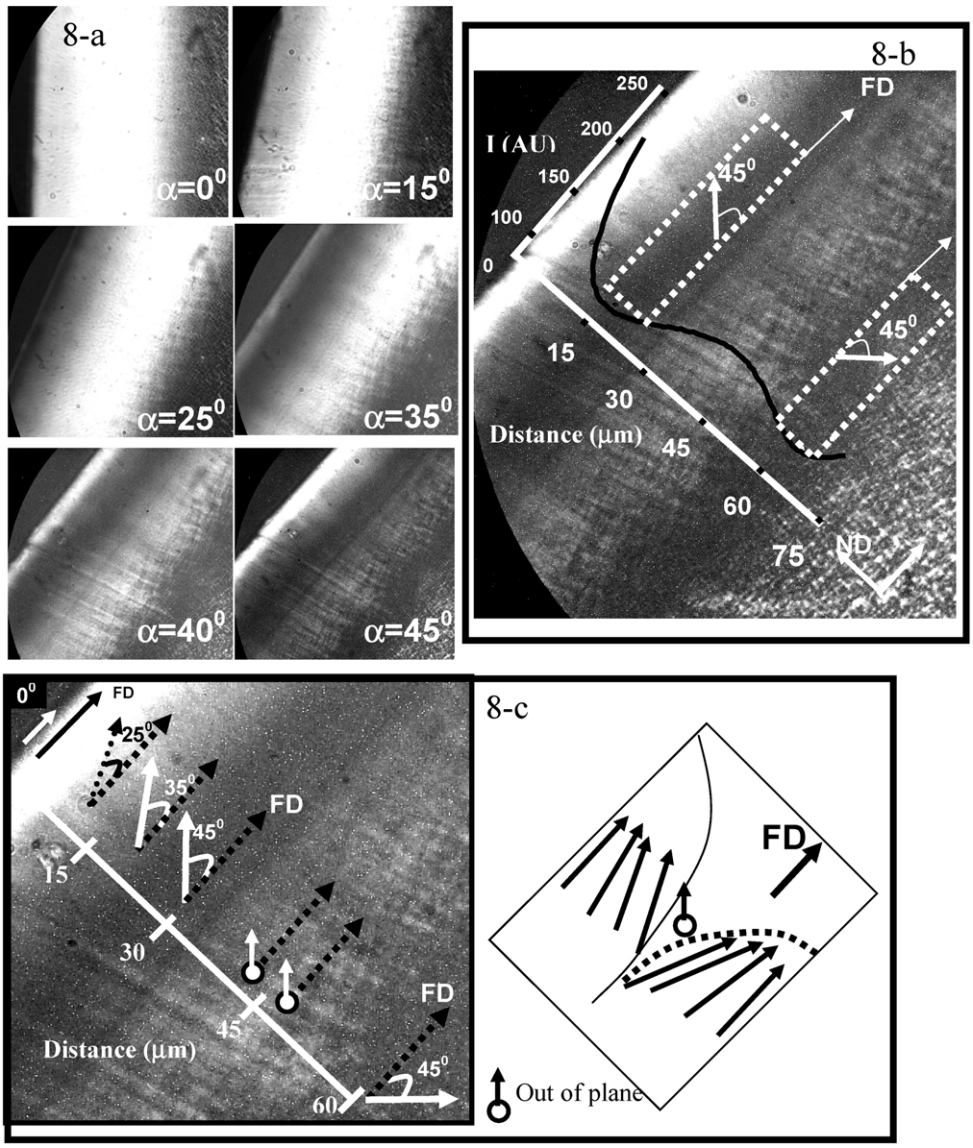

Fig. 8. Optical polarization behavior of the first layer of unfilled nylon 6 at various rotations. α : angle between FD and polarizer.

Spherulite development from flared rod to intermediate sheaf and final complete spheroids was explained and demonstrated in detail in Refs. [38,39]. Under cross-polarized condition such intermediate sheaf-like structures represented by the A, B, C, D and E regions in Fig. 9 allow light transmission through A, B, C and D resulting in four leaf clover type patterns when their long axes are parallel to one of the polarization directions of polarizers. On the other hand, when the long axis is at 45° to the cross-polarizers, only E transmits light giving rod-like appearance. In Fig. 9(a) the optical micrographs indicates that the optic axis of the sheaf-like structure is parallel to the long axis direction in region E and parallel to the radius in the other regions A, B, C and D. In view of this information, it has been concluded that the second layer is made up of incomplete sheaf-like crystallites oriented with their long axes (E) at 25° to the flow direction. When the flow direction of the sample is at 45 to the cross-polarizers, the long axis of the sheaf-like structure is rotated only 20° with respect to the polarizer. This orientation still results in significant light extinction on the A, B, C and D lobes giving rod-like appearances. In Fig. 9(b) the complete rotation of the sheaf-like structure from 0 to 45 is achieved by rotating the sample's flow direction axis from −20 to 70° with respect to the cross-polarizers. Fig. 9(b) shows a single optical image of a sheaf-like entity changing from a yellow rod-like structure at −20° to a spherulitic blue-yellow structure at 45°, followed by a rod-like blue structure at 70°.

A uniform spherulitic structure with random and undeformed morphology is observed after the second layer for the remainder of the core (third layer). The details of these spherulites are shown in Fig. 10. The spherulites with radial fibrils emanating from the center as well as spherulites without the fibrils are clearly observed.

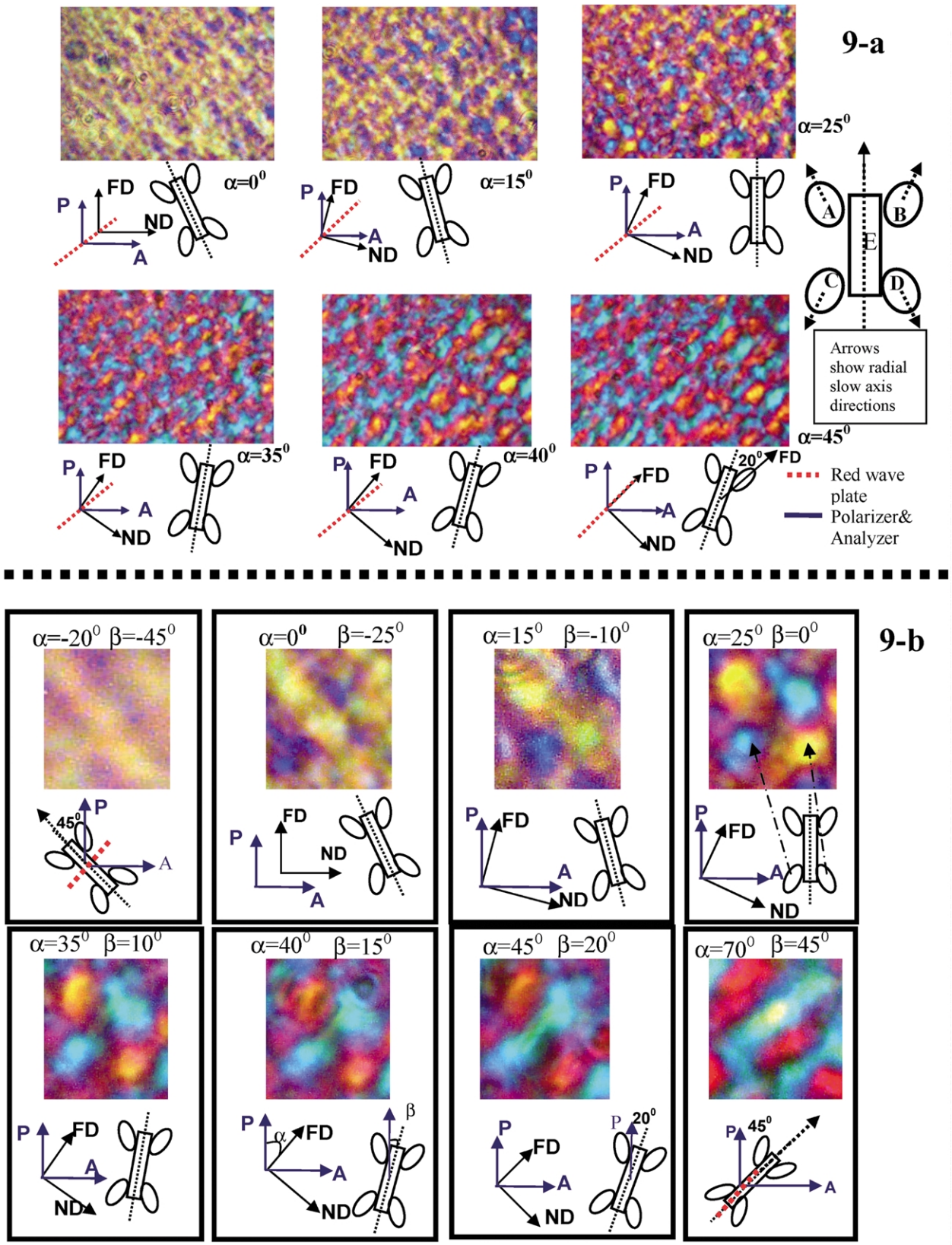

Fig. 9. Optical behavior of second layer of unfilled nylon 6. α : angle between Pol and FD. β : angle between Pol and long axis of the sheaf.

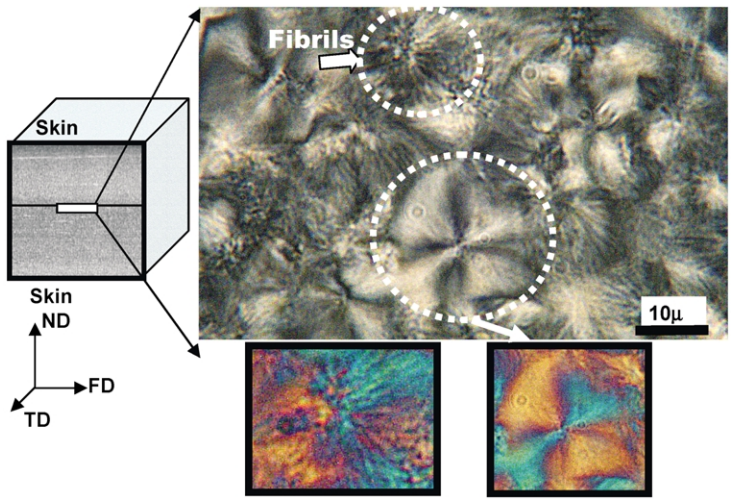

Fig. 10. Polarized optical transmission photomicrographs of B-Cut samples sectioned from the core region of injection molded nylon 6.

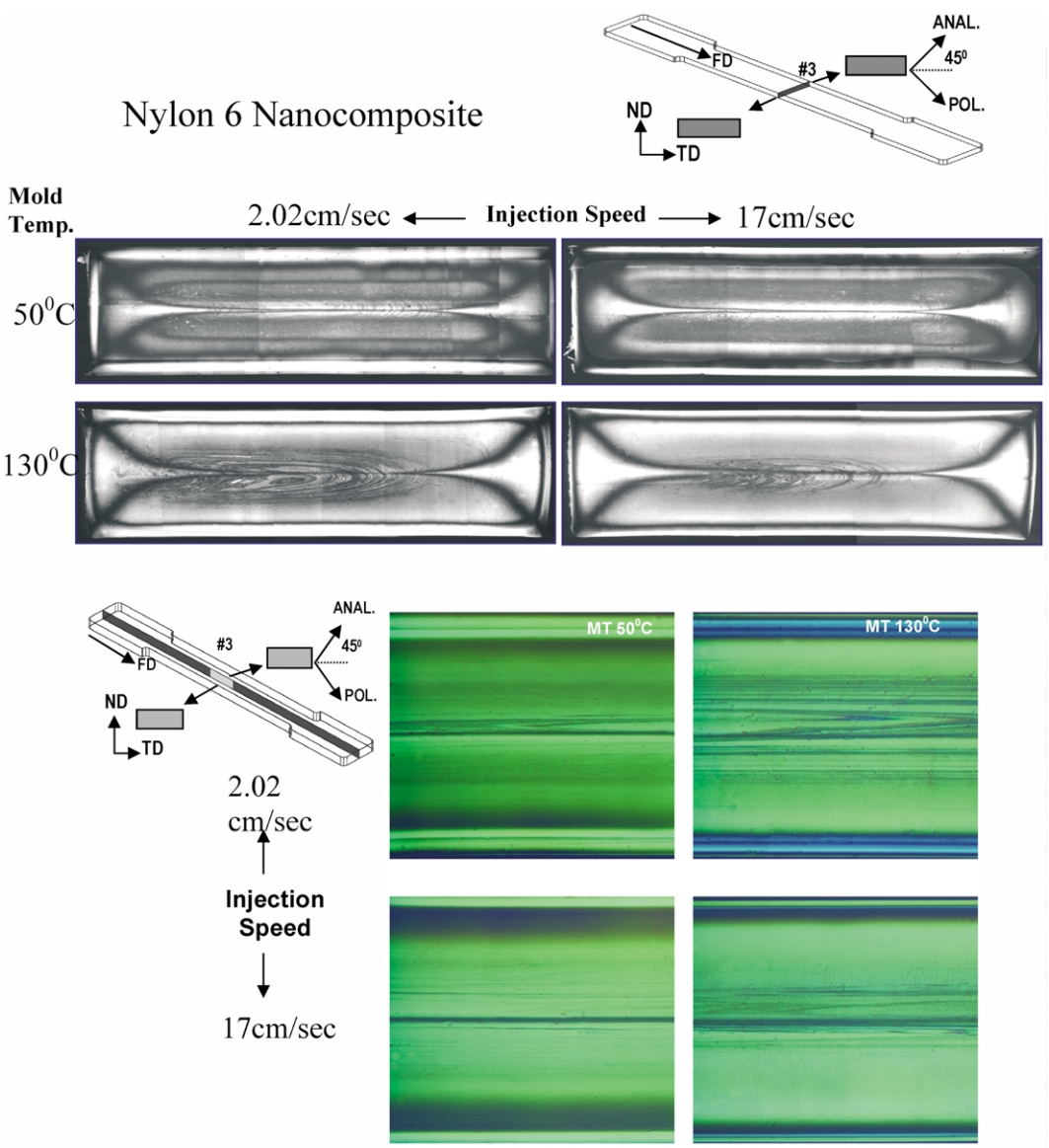

Fig. 11. Polarized optical transmission photomicrographs of A-Cut and B-Cut samples sectioned from injection molded nylon 6 nanocomposite.

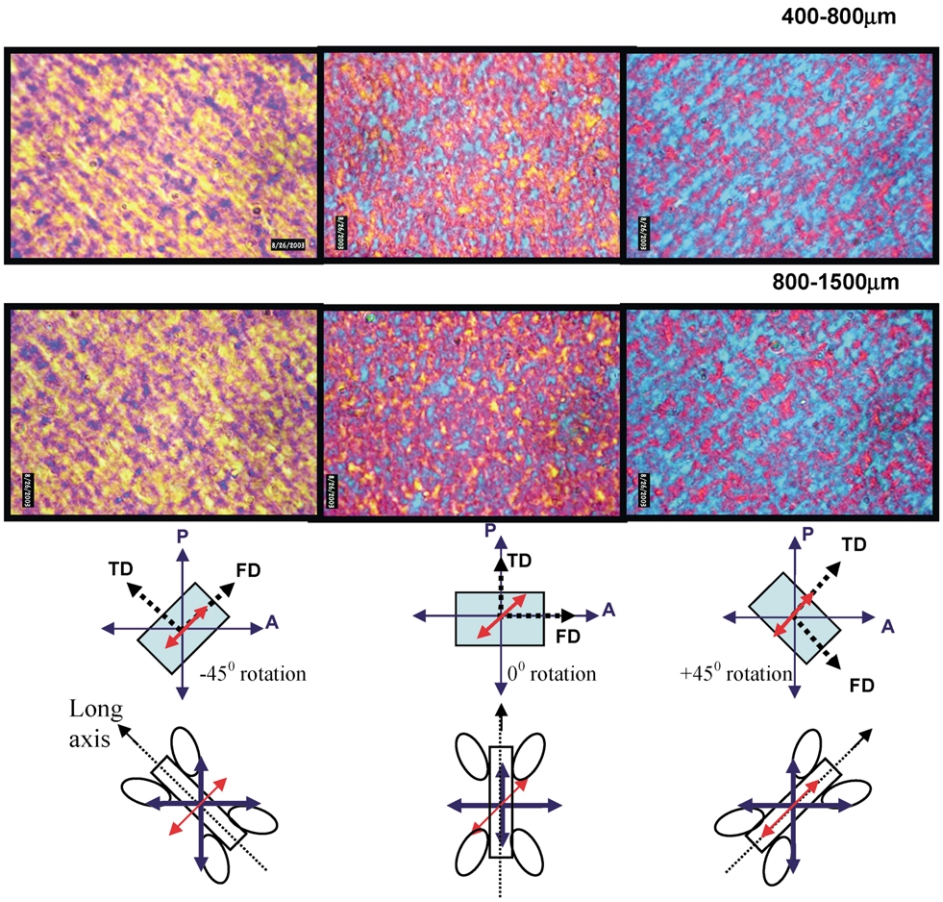

Fig. 12. Polarized optical micrographs of C-Cut samples of nanocomposites at various rotations (red arrow: red wave plate, blue arrows: polarizers, black arrows: FD and TD of the sample).

Cross-sectioning of randomly distributed spherulites causes such morphological differences in the appearance of the spherulites. A cut across the center of a spherulite reveals the fibrils, whereas a cut near the top or bottom of a spherulite hides the fibrils from view. Further details of the spherulites, such as their positively birefringent nature, are revealed when the red-wave plate is inserted. The radial fibrils of the spherulites show dark-light color alternation (either dark-light yellow or dark-light blue depending on the region of the spherulite) in the azimuthal direction indicative of optic axis fluctuation in and out of the radius with a certain angle in the azimuthal direction.

Polarized optical transmission photomicrographs of the A and B-Cut samples sectioned from injection molded nylon 6 nanocomposites are seen in Fig. 11 for two different mold temperatures and injection speeds. The optical photographs of the B-Cut samples with the first order red wave plate reveal a multilayered structure with alternating molecular chain orientation throughout the thickness of the injection molded samples. The optical images show differences with processing conditions, in particular with mold temperature. The increase in injection speed reduces the core area that is covered by alternating dark light sequences.

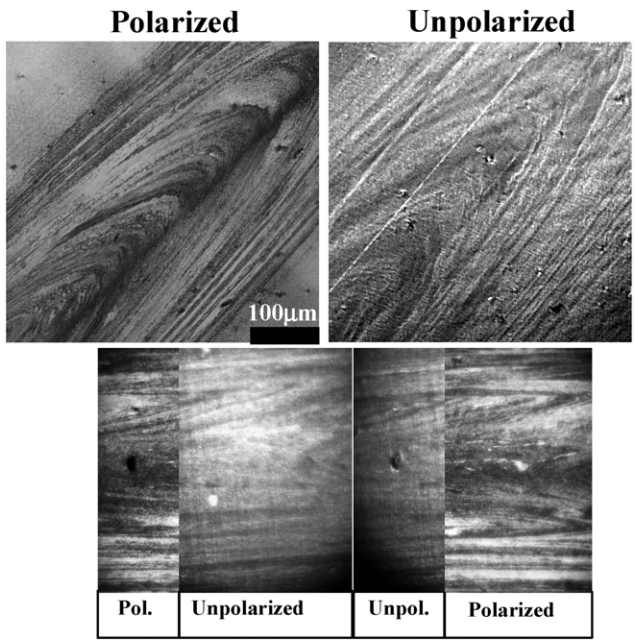

Fig. 13. Polarized optical transmission photomicrograph of flow lines observed in injection molded nylon 6 nanocomposite samples molded at 130 °C (left image is zoomed in).

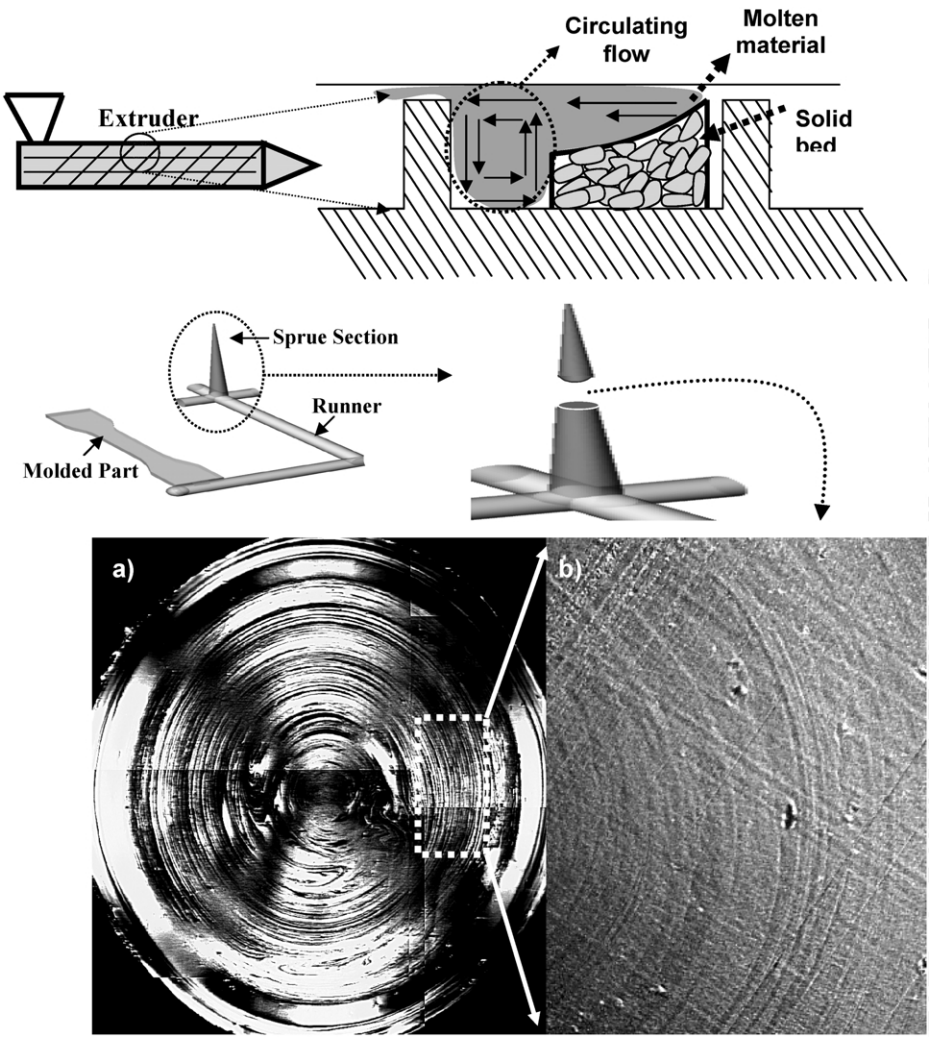

Fig. 14. Polarized optical transmission photomicrographs of A-Cut samples sectioned from sprue to end of cavity in injection molded nylon 6 nanocomposite. (a) Polarized and (b) unpolarized.

As indicated earlier, the 300 μm region consists of two shear layers; first one is formed during injection and the interior formed during creeping flow that takes place during packing [37]. For the rest of the part including the core region, a homogeneous oriented structure similar to the second layer of unfilled nylon 6 prevails. Increased nucleation and lateral crowding interrupts the development of complete spherulites even in the core regions of the samples at a high mold temperature, e.g. 130 °C. Fig. 12 shows the C-Cut nanocomposite samples for the 400–800 and 800–1500 μm regions similar to that applied for the second region of unfilled nylon 6 at relative orientations to polarizers and slow axis of the red wave plate. A transformation from yellow to blue rod-like structure with an intermediate blue-yellow spherulitic morphology is achieved as the microscope stage is rotated from −45 to +45°. This suggests that the structure consists of intermediate sheaf-like entities oriented with their long axis normal to the flow direction. The sheaf-like crystalline superstructures of polybutene-1 films were also reported to be oriented normal to the machine direction [40]. Baranov et al. [41] suggest that the sheaf-like texture results from the anisotropy of crystal growth. Molecular orientation in the melt causes a faster growth of lamellar crystals perpendicular to the flow direction than parallel to it.

4.1.2. Flow lines

In Fig. 13 optical photomicrographs reveal dark line sequences especially in the central core region of nylon 6 nanocomposites at high mold temperatures. Similar flow lines were also observed in the core region of injection molded PBT [42]. In the latter publication, the presence of flow lines was attributed to the rapid solidification of the polymer during filling the mold. Thin sections of thermotropic LCP molded bars and extruded rods also show fine, nematic domains with superimposed flow lines normal to the flow direction, especially near the center of the bar [43]. Similar alternating bands that form under an orientational flow field were reported earlier for injection molded poly(arylene ether ketone) [44].

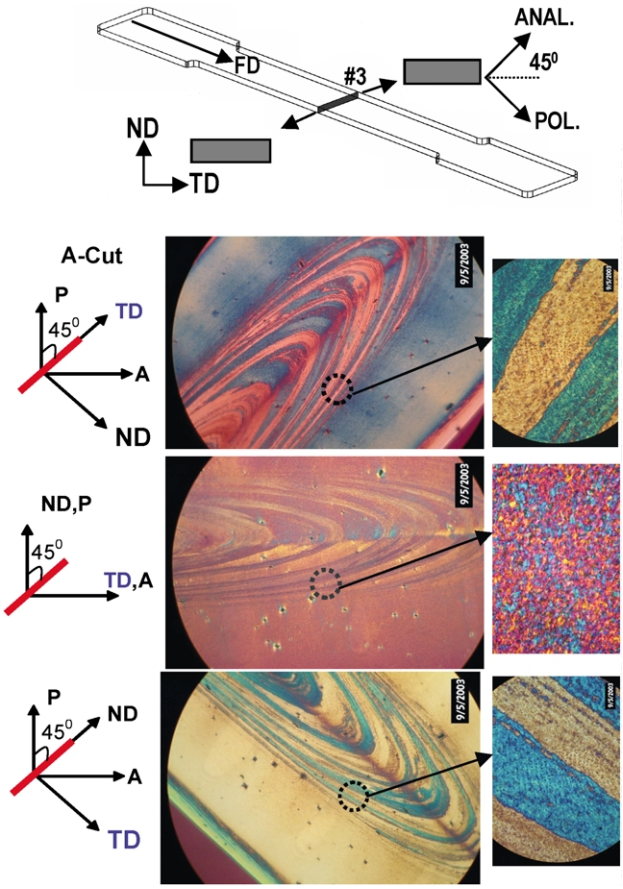

Fig. 15. Anisotropic flow lines on A-Cut samples.

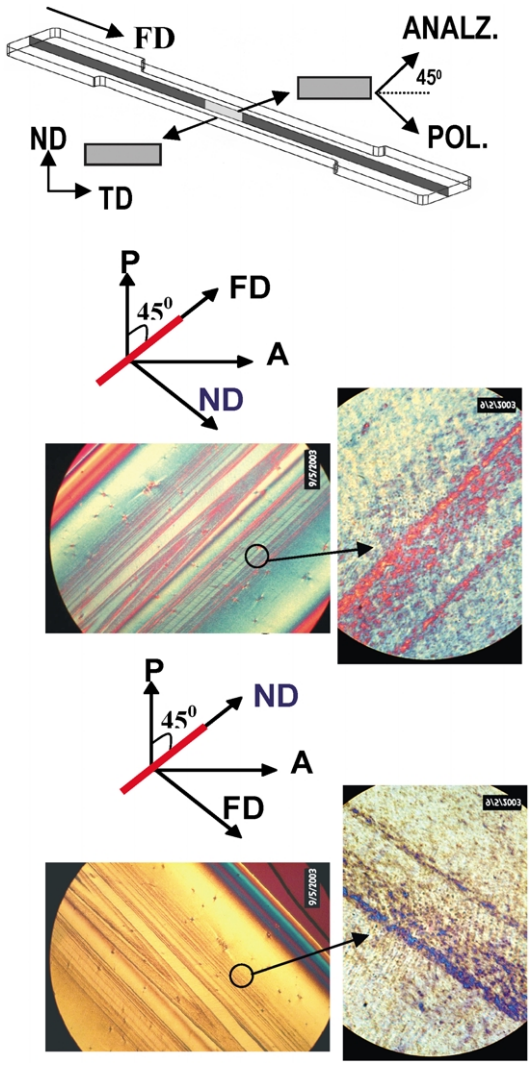

Fig. 16. Anisotropic flow lines on B-Cut samples.

In Fig. 13 both polarized and unpolarized photomicrographs of the same regions are shown in order to distinguish the dark-light layer sequences from the birefringence interference lines. The lines have a parabolic nature and this suggests that they originate because of the circulating motion that is set-up in the melt pool as a result of the screw rotation in the melting zone as depicted in Fig. 14. In order to investigate this possibility, we traced their existence back to the sprue section. In Fig. 14 circular lines exist in the sprue section in both polarized and unpolarized images. Clearly, circular lines undergo certain directional distortions at turn points while flowing from the first runner to the second runner and finally into the cavity, forming the parabolic profile.

To elucidate the anisotropy levels of the layers, a first order red wave plate was inserted in the field of polarization. In Figs. 15 and 16, the birefringence color information suggests that the layers are highly anisotropic and oriented perpendicular to the inter-layer regions. The effect of processing parameters on the flow lines is also investigated. High mold temperature promotes the formation of these lines presumably allowing them to become thicker and more visible with added thermally induced crystallization at these higher temperatures.

In addition to processing conditions, the geometry of the sample also influences the appearance of the flow lines. In certain samples, although the lines are not visible at the entrance and middle region of the samples, they become more substantial further along the flow direction after the diverging section. This suggests that they may be formed by extensional crystallization and carried downstream. In view of the above observations, the flow lines possibly represent threads formed by the unmelted nylon 6 crystals during the melting and conveying stage of the process. Nylon 6 has an equilibrium melting temperature of about 273 °C and the melt temperature employed during injection molding was 250 °C. There also exists a strong possibility that these threads form from melt during the shearing process and transported downstream surrounded by the fast moving melt. These threads act as nucleation sites on which the crystallites grow and cause scattering of light to appear darker in unpolarized light conditions. At high mold temperatures, they become visible as they become large enough to scatter light. Under polarized light conditions, they appear highly oriented attesting to their oriented crystalline nature. In slow crystallizing polymers they were

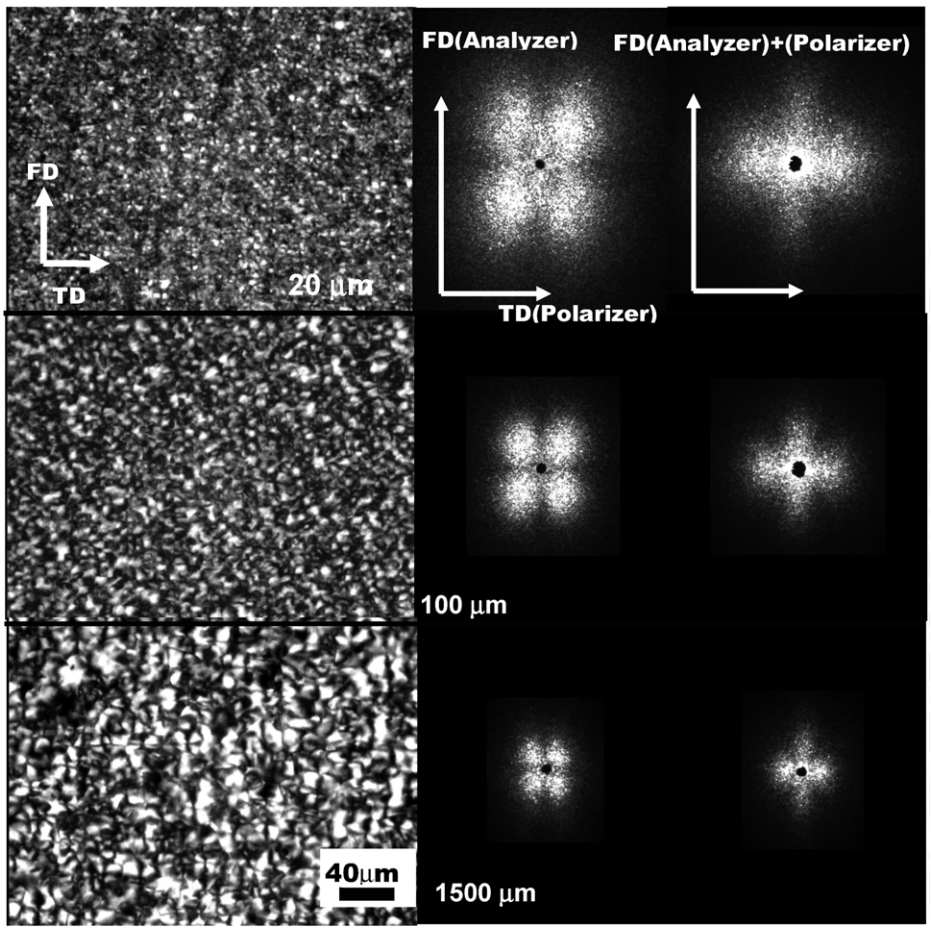

Fig. 17. SALS Hv and Vv patterns of C-cut samples sectioned from unfilled nylon 6 (MT: 130 °C, IS 2.02 cm/s). Left: polarized optical microscopy, middle: Hv patterns, right: Vv patterns.

shown to be crystalline surrounded by amorphous vitrified polymer [44].

The only mechanism that explains this stratified structural behavior is the formation of these oriented crystalline threads upstream by one or both mechanisms described above and transported downstream. If one were to utilize local thermomechanical arguments, one should not observe such inhomogeneous structural gradient.

4.2. Small angle light scattering

Small angle light scattering (SALS) was performed in order to determine the nature, i.e. shape and size, of the crystalline superstructure for unfilled nylon 6 and the nanocomposites. C-cut samples are suitable for SALS experiments, since they allow accurate mapping of the morphological gradient along the ND of the injection-molded bar. This procedure also allows us to quantitatively determine the shape and the size of the spherulites in the FD–TD plane. In the past, we have used the same methodology to map the superstructure profile across the thickness of the PVDF and PVDF/PMMA blends and assess the effect of blend composition on morphological gradients [45].

In Figs. 17 and 18 SALS patterns are shown for unfilled nylon 6 molded at 130 and 50 °C, respectively. In Fig. 17 Hv patterns have azimuthal scattering maxima (μ) at 45° to the polarization directions throughout the thickness of the sample indicative of undeformed spherulitic morphology. This kind of scattering is well understood [46] and was quantitatively explained on the basis of scattering from an anisotropic sphere, in which the optic axis makes an angle of 90° (or 0°) to the radius and orients randomly about the radius.

Similar Hv patterns are seen in the 130–1500 μm region (third layer) of the samples molded at 50 °C. In the 60–130 μm region (second layer), on the other hand, the azimuthal scattering maximum becomes smaller than 45° (μ). This decrease is attributed to the scattering from incomplete sheaf-like structures (sheaves) that were simulated using the fan model by Hashimoto [40]. The origin of the elongated SALS pattern is explained in Fig. 19. The fan angle, the radius of the sheaves and the resultant SALS pattern depend on the crystallization conditions, shear

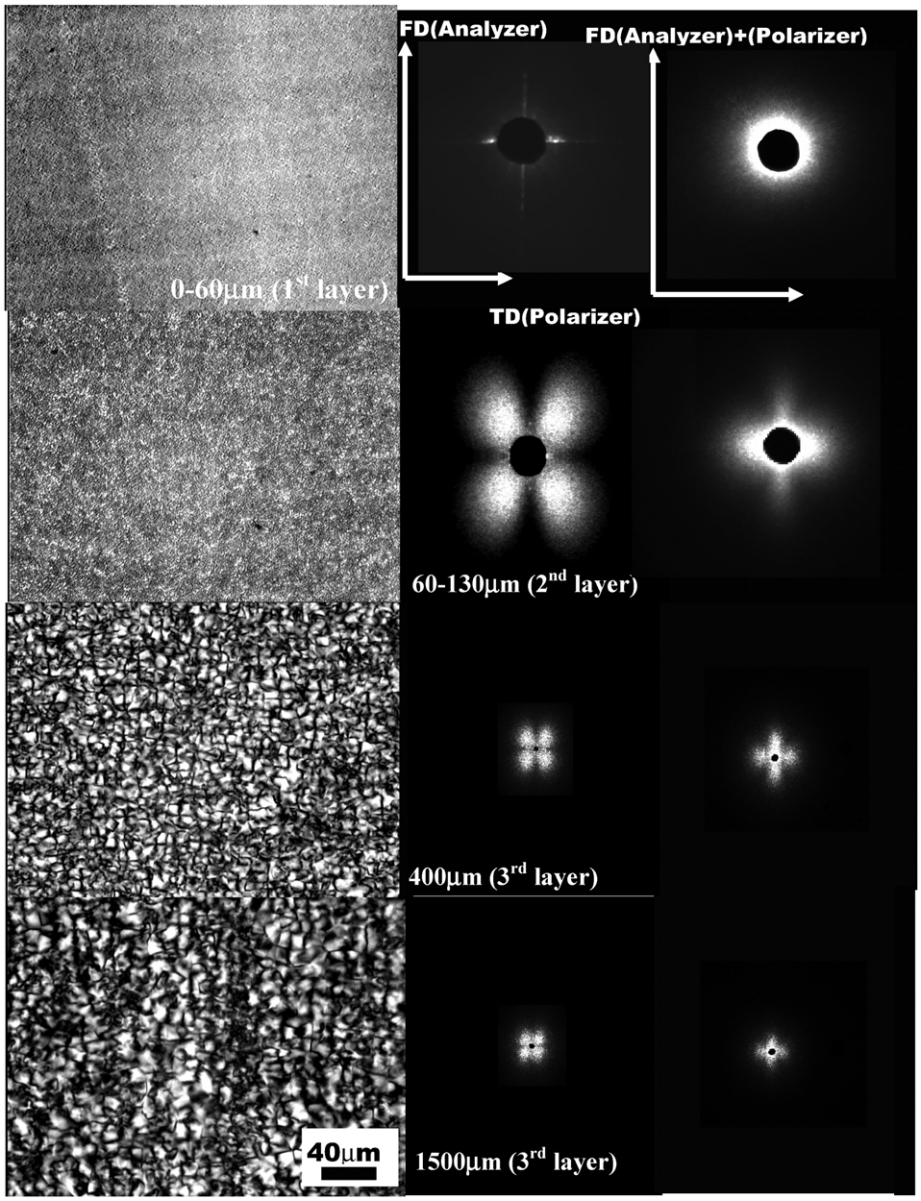

Fig. 18. SALS Hv and Vv patterns of C-cut samples sectioned from unfilled nylon 6 (MT: 50 °C, IS: 2.02 cm/s). Left: polarized optical microscopy, middle: Hv patterns, right: Vv patterns.

stress, and temperature. The fan angle of the sheaf is small at the early stages of crystallization, giving an elongated SALS pattern and decreases further with increasing shear stress.

In the 0–60 μm region (first layer) no intensity can be observed from Hv scattering. This is expected, since the intensity in the Hv mode (Eq. (3.1)) depends only on the radial and tangential polarizabilities ($\alpha_r - \alpha_t$) of the material and its value is low at the low degree of crystallinity of the spherulites that are frozen at the early stages of crystallization near the cold surface. The spatial variation of the Vv patterns from skin towards the core in Fig. 20 also supports this behavior and essentially replicates the temporal evolution of Vv patterns observed during isothermal crystallization of polyethylene [46,47]. The first two terms $I_{V_{v1}}$ (Eq. (3.3)) and $I_{V_{v2}}$ (Eq. (3.4)) in the general I_{V_V} equation (Eq. (3.2)) dominate near the cold surface regions and the scattering is isotropic (circular) (H_H pattern also was observed to be isotropic). With further crystallization towards the core regions, internal anisotropy of the spherulites develops and the third term (Eq. (3.5)) increases leading to the azimuthally dependent Vv scattering. For instance Vv patterns in the interior regions in Fig. 17 represent anisotropic positive spherulites of nylon 6 surrounded in an isotropic medium, i.e. a medium with an equivalent number of spherulites in all directions. The optical sign of the spherulites was determined from polarized optical microscopy by a red-wave plate and remained unchanged from the skin to core regardless of the

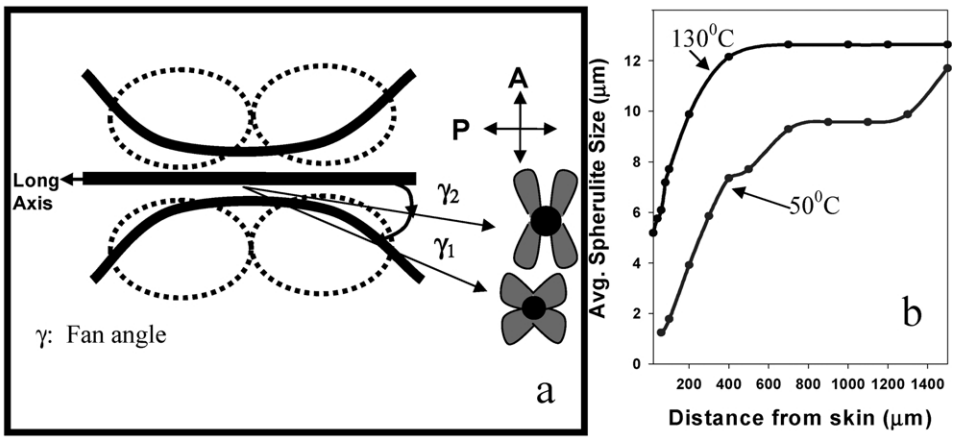

Fig. 19. (a) Change in the shape of Hv SALS patterns from sheaf-like entities with change in aperture angle. (b) Average size of the spherulites for 50 and 130 °C mold temperature.

processing conditions:

$$I_{H_v} = A\rho^2 V_0^2 (3/U^3)^2 \{(\alpha_r - \alpha_t)[\cos^2(\theta/2)/\cos\theta]\sin\mu \cos\mu^*(4\sin U - U\cos U - 3SiU)\}^2)\}^2 \quad (3.1)$$

$$I_{V_{v1}} = I_{V_{v1}} + I_{V_{v2}} + I_{V_{v3}} \quad (3.2)$$

$$I_{V_{v1}} = (\alpha_r - \alpha_s)^2 A\rho^2 V_0^2 (3/U^3)^2 (SiU - \sin U)^2 \quad (3.3)$$

$$I_{V_{v2}} = (\alpha_t - \alpha_s)^2 A\rho^2 V_0^2 (3/U^3)^2 (2\sin U - U\cos U - SiU)^2 \quad (3.4)$$

$$I_{V_{v3}} = (\alpha_r - \alpha_t)^2 A\rho^2 V_0^2 (3/U^3)^2 [\cos^2(\theta/2)/\cos\theta]^2 \cos^2\mu^*(4\sin U - U\cos U - 3SiU)^2 \quad (3.5)$$

where I is the intensity, V_0 is the volume of the anisotropic sphere, θ and μ are the radial and azimuthal scattering angles, A is a proportionality constant and the α_r, α_t, α_s are the radial, tangential and surrounding medium polarizability terms, respectively. ρ is a geometric polarization correction term defined as

$$\rho = \cos\theta(\cos^2\theta + \sin^2\theta\cos^2\mu)^{-1/2} \quad (3.6)$$

SiU is the sine integral defined by

$$SiU = \int_0^U (\sin x/x)\mathrm{d}x \quad (3.7)$$

and is solved as a series expansion sum for computational purposes. The shape factor is

$$U = (4\pi R_0/\lambda')\sin(\theta/2) \quad (3.8)$$

λ' denoting the wavelength of the light in the medium.

The intensity of Hv patterns in Figs. 17 and 18 passes through a maximum at a θ characteristic of the spherulite size. The size of the spherulites is plotted in Fig. 19(b). The size of the spherulites increases towards the interior of the sample as a result of decrease in cooling rates experienced. The size increase in the spherulites can also be observed from the A-cut optical image taken from skin to core in Fig. 7.

In Fig. 21, SALS patterns are shown for injection-molded nylon 6 nanocomposites molded at 130°. Vv patterns are fairly isotropic near the surface regions and this component is prevalent throughout the thickness with some anisotropic components superposed at various depths. Due to increased nucleation effect of the nanoparticles, the formation of complete spherulites with built-in internal anisotropy is suppressed and isotropic component dominates even close to the core regions. This is also true at 50 °C mold temperature.

The shape and the nature of the Hv and Vv patterns of the nanocomposites are not affected by the mold temperature. The Hv patterns will only be discussed for sample molded at 50 °C. It is evident in Fig. 22 that the incorporation of

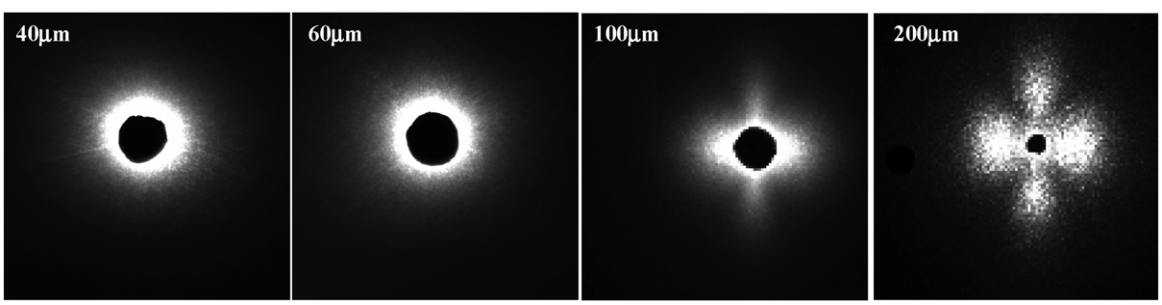

Fig. 20. SALS Vv patterns of unfilled nylon 6 showing transition from isotropy to anisotropy (MT 50 °C, IS 2.02 cm/s).

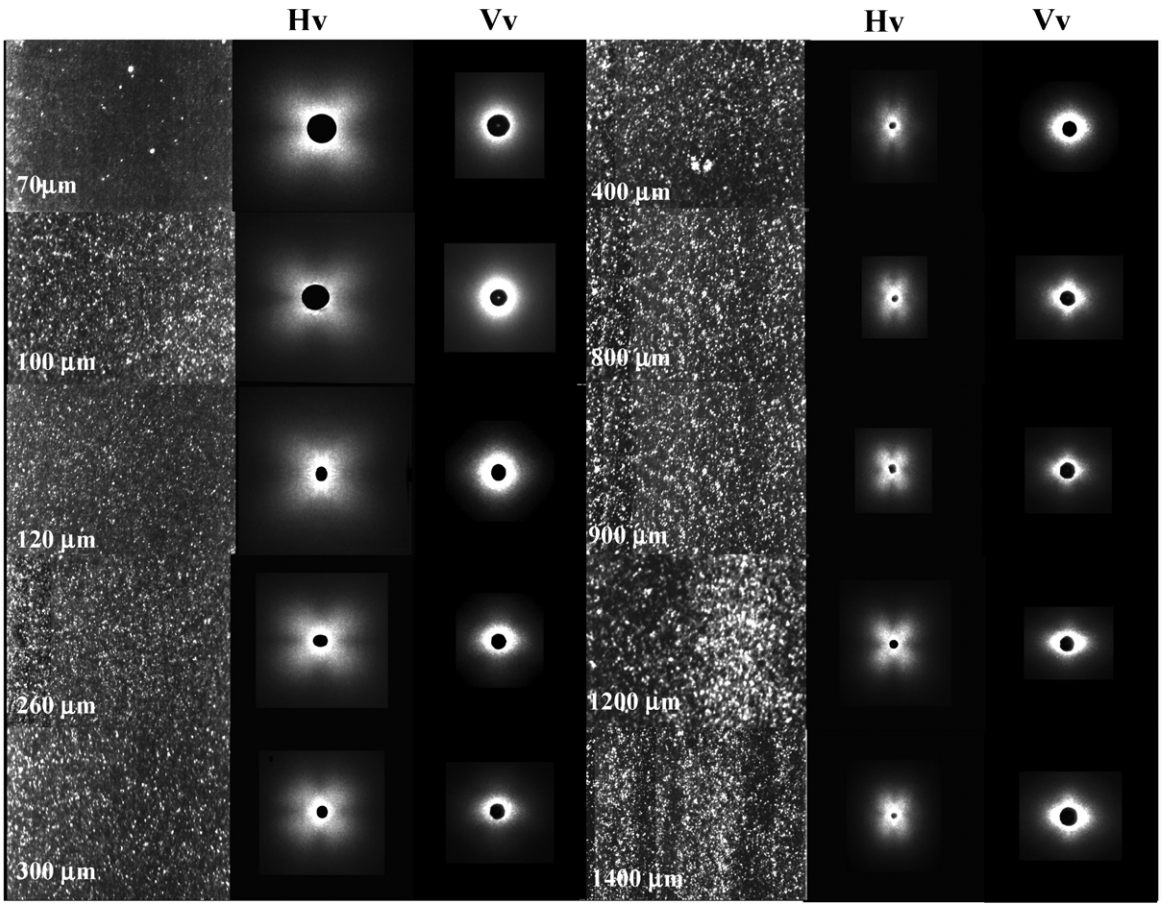

Fig. 21. SALS Hv and Vv patterns of C-cut samples sectioned from nylon 6 nanocomposite (MT 130 °C; IS 2.02 cm/s).

nanoplatelets has changed the typical undeformed clover-leaf scattering patterns to a composite of two patterns in (400–1500 μm) range. There is a small central cross-type pattern with scattering maxima at 0 and 90° to the polarization directions with scattering lobes lying in the direction of polarization. Superposed to this pattern is a larger low intensity pattern with an Hv maximum located at each quadrant. The cross-type Hv pattern (0–90°) was reported earlier by Rhodes and Stein for scattering from both polytetrafluoroethylene (PTFE) rod-like structures [48] and also spherulites [49] for which the optic axis makes an angle of about 45° (nominal value meaning close to 45° rather than 0 or 90°) to the length of the rod and the spherulite radius, respectively. The nature of this kind of Hv scattering was simulated by the theory of spherulite scattering with an arbitrary optic axis orientation angle, β [50] and the more general theory of the scattering from media having nonrandom orientation correlations [51]. Both types of theories predict that Hv patterns must either be of the 0–90 or 45° type, depending on the relative orientations of the principal polarizability direction and the maximum dimension (or direction of maximum correlation) for the structure. Stein earlier observed single 0, 90° scattering streaks, as well as superimposed 0, 90 and 45° streaks from PCTFE copolymer films during the course of isothermal crystallization, characteristic of the development of sheaves as observed microscopically [38]. However, the second region of unfilled nylon 6, although made up of similar intermediate sheaf-like structures, does not show such central scattering patterns. Therefore, the presence of the sheaves alone cannot explain the formation of such scattering patterns. Their short and the long-range spatial organization along with the optic axis orientation should be taken into account. In order to elaborate on the origin of these superimposed light scattering patterns, let us first consider the outer large pattern (see Fig. 22). Scattering at large angles is attributed to scattering from smaller entities in real space, these small entities being the sheaves. In the 400–800 μm region, the fan angle of the sheaf is smaller compared to the 800–1500 μm region. Due to high nucleation density closer to the surface, the sheaves are frozen in at the earlier stages and the splaying of the fibrils from rod-like bundles is suppressed under rapid solidification in these regions. Previously, we have illustrated that smaller fan angles result in the elongated patterns with the azimuthal angle of less than 45° (see Fig. 19).

The small central scattering (0–90°) pattern on the other hand has the same nature for both the 400–800 μm and the 800–1500 μm region. Possibly, it arises from the alignment

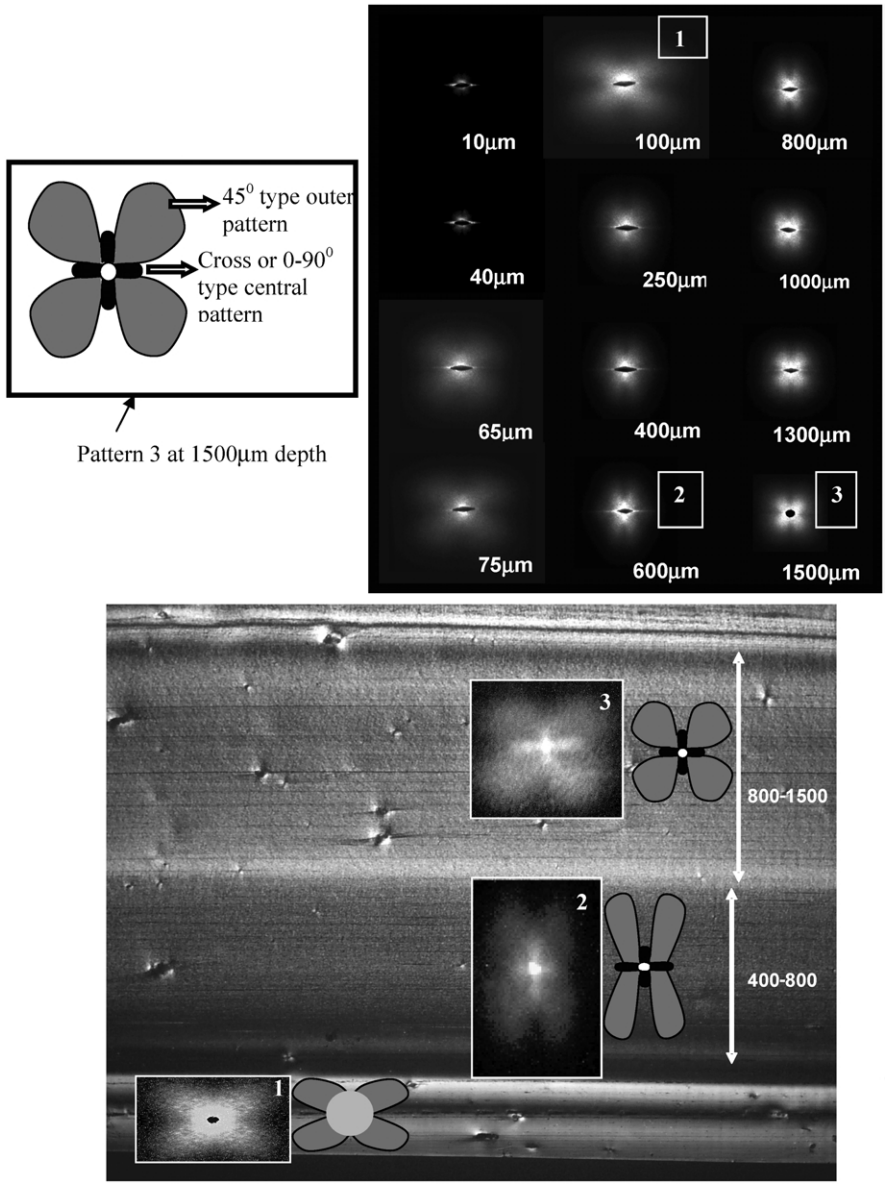

Fig. 22. SALS patterns along the thickness of nylon 6 nanocomposite molded at 50 °C.

of the sheaves, which results in large rod-like structures where the optic axes of the sheaves are at an angle between 0 and 90° to the rod axis. A model for the 400–800 and 800–1500 μm region depicts the alignment of the sheaves and the resulting SALS patterns in Fig. 23.

The top 75–200 μm region of the nanocomposites display large elongated rod-like scattering patterns that show decreasing intensity at large scattering angles, indicating the presence of very small oriented threads. These threads are formed under high shear forces exerted by the solid–liquid boundary as well as the nanoparticles. Increased deformation and fast cooling rates increase the nucleation density and the formation of small threads in large quantities. The Vv patterns in this region are slightly dependent on the azimuthal direction indicating that the significant internal anisotropy did not develop.

The outmost surface region, 0–75 μm does not display any Hv scattering as the structure of the material is frozen in at the very early stages of crystallization where the anisotropy has not developed at all. The circular Vv patterns also support this observation.

4.2.1. Summary of structural hierarchy

Figs. 24 and 25 summarize the structural observations for unfilled nylon 6 and nylon 6 nanocomposite, respectively.

Injection molded nylon 6 exhibit mainly three different morphological regions from skin to core as shown in Fig. 24.

The first layer is a 60 μm shear layer that captures the geometrical features of the development of solidified layer during injection and parabolic profile of the shear field. Near the skin the local symmetry axes are tilted towards the skin

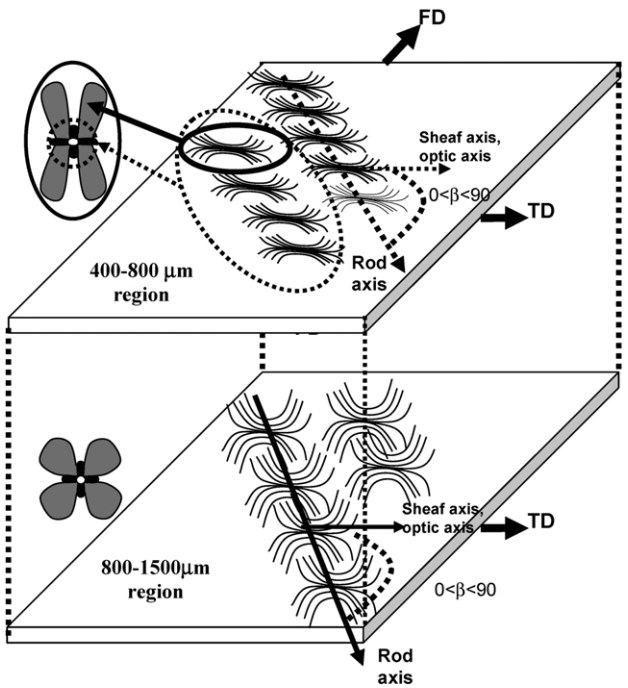

Fig. 23. Origin of complex light scattering patterns.

following the contour of the leading edge of solid–liquid boundary. Towards the middle region, it starts to move out of the FD–ND plane and back into the plane further in the interior following the parabolic profile of the governing shear field. In this region, rapid cooling suppresses the orientation relaxation thereby capturing the parabolic shear profile.

The second layer that forms during creeping flow of packing state is 70 μm thick and made up of intermediate sheaves that are the precursors of complete spherulites. Birefringence color information from a first order red wave plate in the field of polarization was effective in the interpretation of the sheaves. The sheaves are oriented with their long axis 25° to the flow direction. Fig. 24 shows a single sheaf appearing as a blue rod when the long axis of the sheaf is parallel to the red wave plate and at 45° to the cross-polarizers.

The development of full spherulites follows immediately in the third layer and prevails for the most part of the molded part (130–1500 μm). Towards the core regions, the size of the spherulites increases from about 2 to 12 μm as a result of the decrease in cooling rates.

The morphological transformations that form during the temporal evolution of the spherulites are spatially mapped to the structural gradient from skin to core in the injection molded parts. This is also evidenced by the SALS

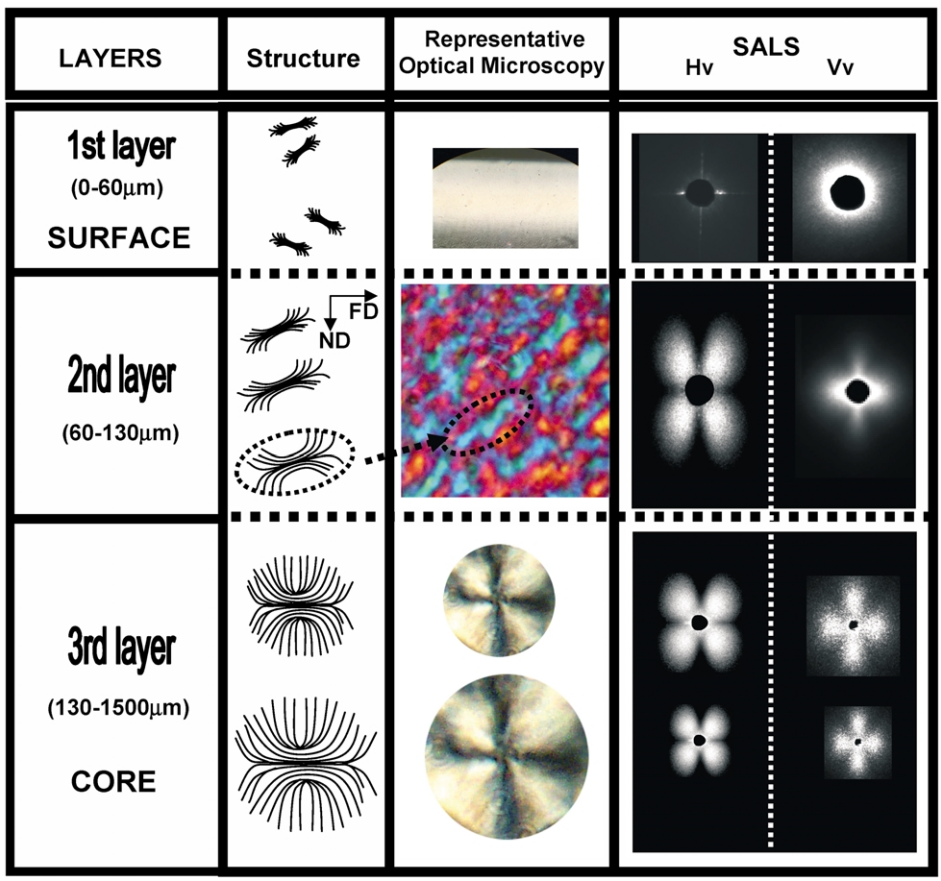

Fig. 24. Spatial variation of structure developed in unfilled nylon 6.

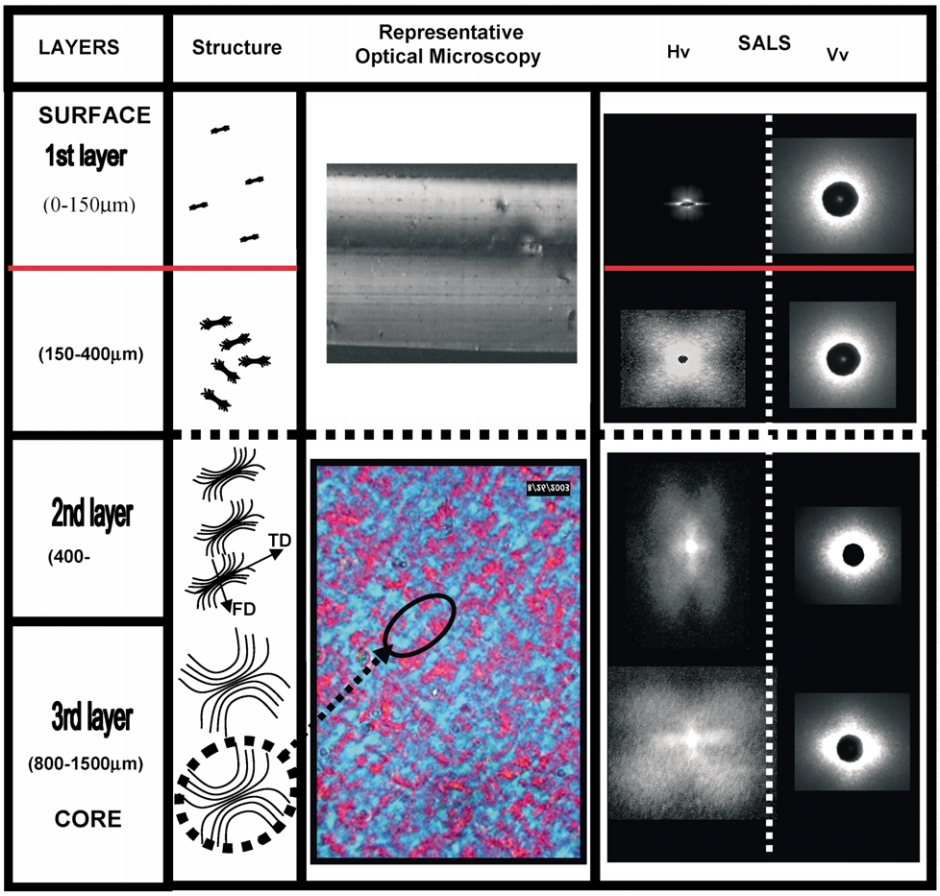

Fig. 25. Spatial variation of structure developed in nylon 6 nanocomposites.

experiments where isotopic Vv patterns, that appear circular, change into anisotropic Vv patterns further in the interior of the part. In general, nylons [52] are characterized by overall rates of crystallization that are intermediate between, for example, fast-crystallizing polyethylene and easily quenchable PET. In slow crystallizing polymers, such as PEN [53–55], PEEK [56,57], PAEK [45], etc. the thermally crystallized layers can only be observed in the core region of the samples when molded at temperatures above their glass transition temperature. In addition, due to their slow crystallizing character, the crystallites are frozen in at the very early stages of their development, made up of rod-like crystals similar to what we observe in the outer most first layer of unfilled nylon 6. In the case of fast crystallizing polymers such as PP [37], PE, etc. the crystallization occurs so rapidly that we can only see the full spherulites that form by thermal crystallization. In unfilled nylon 6, we observe all the stages of the development of spherulites from initial crystal bundles, to intermediate sheaves and finally full spherulites.

In nylon 6 nanocomposite molded parts, on the other hand, due to the coupled effect of increased nucleation sites offered by the nanoplatelets and the deformation taking place in between these layers, the formation of full spherulites are interrupted even in the core regions. Although crystallization rates are faster for nanocomposites than the unfilled samples, spherulitic development is stopped by the lateral crowding and impingement of the sheaves. As evidenced by the SALS and the optical microscopy, the nanocomposite samples exhibit mainly sheaves with increased splaying morphology towards the interior covering most of the molded part (400–1500 μm). The regions near the surface exhibit shear crystallized oriented structures. The anisotropy of the Vv patterns increase towards the core but never reaches to that of unfilled nylon 6 even at high temperatures (compare Vv for unfilled and nanocomposite in Figs. 17 and 21, respectively).

5. Conclusions

Nanoplatelets induce high levels of orientation of the polymer matrix throughout the thickness of the molded part even at high mold temperatures where nonisothermal effects are highly suppressed and confined to very close proximity of surfaces. Through orientation of the molecules and the foreign particle effect of the nanoplatelets, the nucleation density is increased and complete spherulitic formation is suppressed even in the core regions at high mold temperatures. The sheaves that develop in the intermediate

stages of spherulite evolution prevail in the most part of molded part.

Acknowledgements

We would like to thank Dr Kris Akkapeddi of Honeywell who has kindly provided the materials.

References

[1] Usuki A, Kojima Y, Kawasumi M, Okada A, Fukushima Y, Kurauchi T, Kamigaito O. J Mater Res 1993;6:1185–9.
[2] Kojima Y, Usuki A, Kawasumi M, Okada A, Kurauchi T, Kamigaito O. J Polym Sci: Part A 1993;31:983–6.
[3] Kojima Y, Usuki A, Kawasumi M, Okada A, Kurauchi T, Kamigaito O. J Polym Sci: Part A 1993;31:1755–8.
[4] Liu LM, Qi ZN, Zhu XG. J Appl Polym Sci 1999;71:1133–8.
[5] Lan T, Kaviratna PD, Pinnavaia TJ. Chem Mater 1994;6:6573–5.
[6] Gilman JW, Morgan A, Giannelis EP, Wuthenow M, Manias E. Flame Retardancy 10th Annual BBC Conference Proceedings; May 1999. p. 1–11.
[7] Giannelis EP. Advanced Materials 1996;8:29.
[8] Ergungor Z, Cakmak M. Macromol Symp 2002;185:259–76.
[9] Kojima Y, Usuki A, Kawasumi M, Okada A, Kurauchi T, Kamigaito O, Kaji K. J Polym Sci: Part B 1995;32:625–30.
[10] Kojima Y, Usuki A, Kawasumi M, Okada A, Kurauchi T, Kamigaito O, Kaji K. J Polym Sci: Part B 1995;33:1039–45.
[11] Kuchta FD, Lemstra PJ, Keller A, Lawrence FB, Fischer HR. Mater Res Soc Symp Proc 2001;628:CC11.12.1–CC11.12.7.
[12] Nam PH, Maiti P, Okamoto M, Kotaka T, Hasegawa N, Usuki A. Polymer 2001;42(23):9633–40.
[13] Fujiwara S, Sakamoto T. Japanese Pat. 1976; Jp-A-51-109998.
[14] Alexandre M, Dubois P. Mater Sci Engng 2000;28:1–63.
[15] Usuki A, Kojima Y, Okada M, Kurauchi T, Kamigaito O, Deguchi R. Polym Prepr Jpn 1990;39:2427.
[16] Usuki A, Kojima Y, Kawasumi M, Okada A, Fukushima Y, Kurauchi T, Kamigaito O. J Mater Res 1993;8:1179–83.
[17] Usuki A, Kawasumi M, Kojima Y, Okada A, Kurauchi T, Kamigaito O. J Mater Res 1993;8:1174–8.
[18] Liu LM, Qi ZN, Zhu XG. J Appl Polym Sci 1999;71:1133–8.
[19] Fukushima Y, Okada A, Kawasumi M, Kurauchi T, Kamigaito O. Clay Miner 1988;23:27–34.
[20] Pinnavaia TJ, Beall GW. Polymer–clay nanocomposites, 1st ed. New York: Wiley; 2001.
[21] Yang F, Ou Y, Yu Z. J Appl Polym Sci 1998;69:355–61.
[22] Russel PD, Beaumont WRP. J Mater Sci 1980;15:197–207.
[23] Zdenek M, Chompff JA. J Polym Sci: Part B 1974;12:977–89.
[24] Varlot K, Reynaud E, Loppfer MH, Vigier G, Varlet J. J Polym Sci: Part B 2001;39:1360–70.
[25] Yalcin B, Cakmak M. Polymer 2003;44:6913–25.
[26] Hsiung CM, Cakmak M. Int Polym Progressing 1993;8(2):164–77.
[27] Hsiung CM, Cakmak M. Int Polym Progressing 1993;8(3):255–70.
[28] Keuchel K. MS Thesis. Akron, OH: Polymer Engineering, University of Akron; 1994.
[29] Kojima Y, Matsuoka T, Takahashi H, Kurauchi T. J Appl Polym Sci 1994;51:683.
[30] Es MVA. PhD Thesis. Delft, the Netherlands: Delft University of Technology; 2001.
[31] White TR. Nature 1955;175:895.
[32] Liu L, Zhu X, Qi Z. Gaofenzi Xuebao 1999;3:274.
[33] Wu T, Liao C. Macromol Chem Phys 2000;201:2820.
[34] Todoki M, Kawaguchi T. J Polym Sci, Polym Phys Ed 1977;15:1067.
[35] Itoh T, Miyaji H, Asai K. Jpn J Appl Phys 1975;14:206.
[36] Lincoln DM, Vaia RA, Wang ZG, Hsiao BS, Akkapeddik. Polymer 2001;42:9975–85.
[37] Ayrom-Keuchel H, Cakmak M. ANTEC 1999;2:1910–4.
[38] Adams GC, Stein RS. J Polym Sci 1968;6:31–61.
[39] Morse HW, Donnay JDH. Am Mineral 1936;21:391.
[40] Hashimoto T, Todo A, Murakami Y, Kawai H. J Polym Sci, Phys Ed 1977;15:501–21.
[41] Baranov VG, Volkov TI, Farshyan GS, Frenkel SYa. J Polym Sci C 1968;38:61.
[42] Fitchmun DR, Newman S. J Polym Sci, Polym Lett 1969;7:301.
[43] Sawyer LC, Jaffe M. J Mater Sci 1986;21:1897–913.
[44] Ulcer Y, Cakmak M, Hsiung CM. J Appl Polym Sci 1995;55(8): 1241–63.
[45] Wang YD, Cakmak M. Polymer 2001;42:3731–43.
[46] Rhodes MB, Stein RS. J Polym Sci 1960;31:1873.
[47] Rhodes MB, Stein RS. J Polym Sci 1960;45:521.
[48] Rhodes MB, Stein RS. J Polym Sci 1962;62:S84.
[49] Rhodes MB, Stein RS. Polym Lett 1963;1:663–7.
[50] Clough S, Van Aartsen JJ, Stein RS. J Appl Phys 1965;36:1965.
[51] Stein RS, Erhardt PF, Clough S, Adams G. J Appl Phys 1960;37:3980.
[52] Kohan MI. Nylon plastics, 1st ed. New York: Wiley-Interscience; 1973. Chapter 8.
[53] Ulcer Y, Cakmak M. Polymer 1994;35:5651.
[54] Ulcer Y, Cakmak M. J Appl Polym Sci 1996;62:1661.
[55] Ulcer Y, Cakmak M. Polymer 1997;38:2907.
[56] Hsiung CM, Cakmak M, White JL. Polym Engng Sci 1990;30(16): 967.
[57] Hsiung CM, Cakmak M. J Appl Polym Sci 1993;47:125–49.